Geophysical Journal International

Geophys. J. Int. (2015) **202,** 1122–1136 doi: 10.1093/gji/ggv202
GJI Geodynamics and tectonics

Subduction tractions and vertical axis rotations in the Zagros–Makran transition zone, SE Iran: the 2013 May 11 M_w 6.1 Minab earthquake

Camilla Penney,[1] Alex Copley[1] and Behnam Oveisi[2]

[1]*COMET, Bullard Labs, Department of Earth Sciences, University of Cambridge, Cambridge, United Kingdom. E-mail: cp451@cam.ac.uk*
[2]*Seismotectonics Department, Geological Survey of Iran, Azadi Square, Meraj Blvd, Tehran, Iran*

Accepted 2015 May 12. Received 2015 May 8; in original form 2015 March 3

SUMMARY

The source parameters and slip distribution of the 2013 May 11 M_w 6.1 Minab earthquake are studied using seismology, geodesy and field observations. We observe left-lateral strike-slip motion on a fault striking ENE–WSW; approximately perpendicular to previously studied faults in the Minab–Zendan–Palami fault zone. The fault that ruptured in 2013 is one of a series of ∼E–W striking left-lateral faults visible in the geology and geomorphology. These accommodate a velocity field equivalent to right-lateral shear on ∼N–S striking planes by clockwise rotations about vertical axes. The presence of these faults can reconcile differences in estimates of fault slip rates in the western Makran from GPS and Quaternary dating. The longitudinal range of shear in the western Makran is likely to be controlled by the distance over which the underthrusting Arabian lithosphere deepens in the transition from continent–continent collision in the Zagros to oceanic subduction in the Makran.

Key words: Earthquake source observations; Continental neotectonics; Asia.

1 INTRODUCTION

The 2013 May 11 M_w 6.1 Minab earthquake occurred in the sparsely populated desert to the east of the Strait of Hormuz, in SE Iran (Fig. 1). The earthquake occurred in the western part of the Makran subduction zone, where Arabian oceanic lithosphere is thrust beneath southern Iran and Pakistan. To the west, this oceanic subduction transitions into continent–continent collision in the Zagros mountains of Iran. The Minab earthquake presents an opportunity to address a number of open questions, such as those raised by the M_w 7.7 Balochistan earthquake in 2013; a strike-slip event that ruptured a curved fault at the eastern end of the Makran subduction zone (Avouac *et al.* 2014; Jolivet *et al.* 2014). That event highlighted that the onshore part of the accretionary wedge built above the subduction interface can be seismically active and characterized by strike-slip faulting. We examine the 2013 Minab event to better understand the deformation of the accretionary wedge in the Zagros–Makran transition zone. This earthquake is also important from the perspective of understanding the regional tectonics and distribution of strain in the western Makran, which give insights into both earthquake hazard and the factors controlling the distribution and style of faulting in the continents. This paper addresses these issues by studying the 2013 Minab earthquake using a combination of seismology, satellite geodesy and field observations. We then consider the implications of our results for the driving forces and distribution of faulting in the region.

2 BODY WAVEFORM MODELLING

Teleseismic *P* and *SH* waveforms in the epicentral distance range 30–80° were extracted from the IRIS DMC. The seismograms were deconvolved from their instrument responses and reconvolved with the response of a World-Wide Standardised Seismographic Network Long Period (15–100) seismometer. In this period range, a moderate-size earthquake can be approximated as a point source. *P* and *SH* wave data were then inverted using the MT5 program of Zwick *et al.* (1994) based on the method proposed by McCaffrey & Abers (1988) and McCaffrey *et al.* (1991), for fault plane orientation (strike, dip and rake), source-time function, centroid depth and seismic moment. We use a least-squares fitting algorithm to minimize the point-wise misfit between observed and synthetic seismograms. This procedure requires accurate alignment of the synthetics with *P* and *SH* wave arrivals. Long-period filtering can make impulsive arrivals difficult to observe, so *P* and *SH* arrival times were manually picked in the broad-band data.

Filtering the seismograms to long periods allows moderate-sized earthquakes ($M_w < 7$) to be modelled as point sources with temporally extended source-time functions. This filtering also reduces sensitivity to small-scale variations in velocity structure in the source region. Throughout our seismic and geodetic inversions we use a velocity model in the source area derived from the local earthquake study of Yamini-Fard *et al.* (2007). Our earthquake source models are contained within the uppermost crustal layer of this velocity

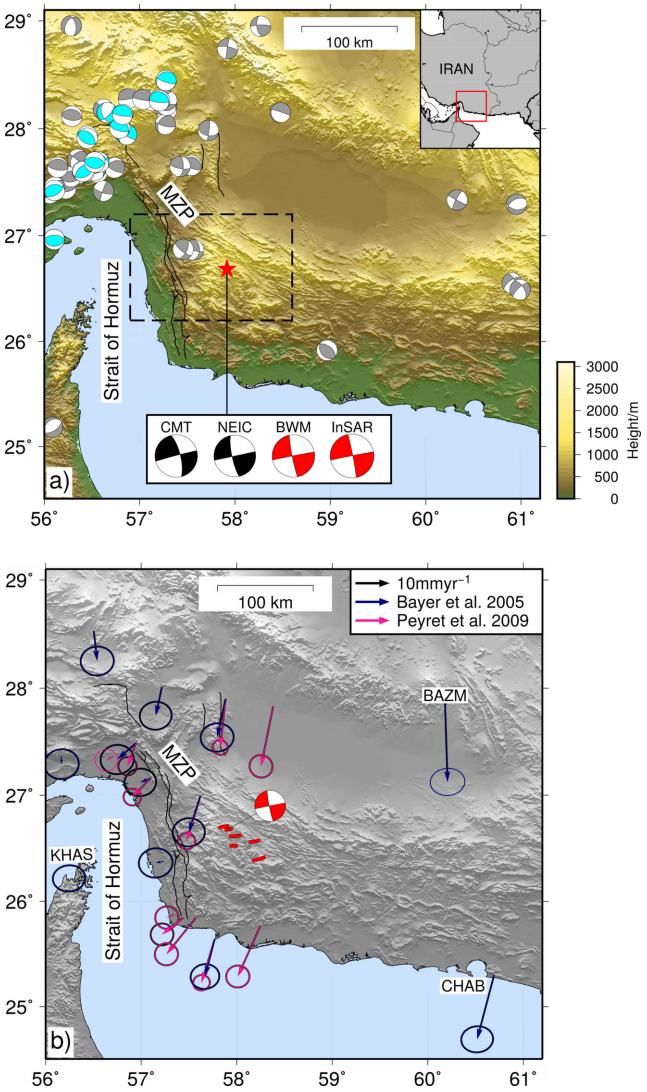

Figure 1. Overview of study area. MZP (black lines) is the Minab–Zendan–Palami fault zone, the trace of which is taken from Bayer *et al.* (2006). (a) shows the regional seismicity. The compressional quadrants of focal mechanisms are shaded. Those in blue are taken from Nissen *et al.* (2011) and have been constrained by body waveform modelling, those in grey are from the gCMT (Dziewonski *et al.* 1981; Ekström *et al.* 2012) catalogue and are located at EHB epicentres until 2009 and NEIC epicentres for later events. Mechanisms to the west are dominantly thrust faulting at the eastern end of the Zagros mountains. Focal mechanisms for the 2013 Minab event are shown boxed, those in red are taken from this study from body waveform modelling (labelled BWM, see Section 2) and constant slip inversion of InSAR data (labelled InSAR, see Section 3). The inset shows location of study in Iran and the dashed box shows the location of Fig. 6(b) shows GPS velocities plotted with respect to Arabia, using the Arabia-Eurasia Euler pole of Vernant *et al.* (2004). Pink arrows are from Peyret *et al.* (2009) and blue arrows are from Bayer *et al.* (2006). Ellipses show 95 per cent confidence intervals. Velocities increase to the east, causing differential shear across the region (see Section 6.1). The focal mechanism for the 2013 Minab earthquake from this study is shown in red. Red lines are faults visible in the geomorphology (see Section 5).

model ($V_p = 5.6$ km s^{-1}, $V_s = 3.3$ km s^{-1} and $\mu = 28.3$ GPa) allowing us to use a uniform half-space as our medium. As observed by Taymaz (1990), the details of the velocity structure had little effect on the derived source parameters using this method, changing them only within the expected errors, which have been extensively discussed in the literature (e.g. Molnar & Lyon-Caen 1989).

Table 1. Source parameters from seismology (BWM) and InSAR inversions.

Method		Strike (°)	Dip (°)	Rake (°)	M_0 (10^{18} N m)
NEIC	Plane 1	258	90	11	1.6
	Plane 2	168	79	178	
CMT	Plane 1	346	74	−178	2.2
	Plane 2	255	88	−16	
BWM	Plane 1	259	89	5	1.7
	Plane 2	169	85	179	
InSAR	Fault plane	259	89	−3	4.4
	Auxiliary plane	349	87	−179	

A subset of seismograms was selected based on visual inspection of the signal-to-noise ratio in both the broad-band and filtered records. The gCMT solution (Table 1; Dziewonski *et al.* 1981; Ekström *et al.* 2012) was used as the starting model. The source-time function was composed of triangular elements of half-duration 2 s, using a sufficient number of elements that the total duration was not artificially imposed in the inversion. The source was constrained to be pure double-couple. Seismograms were weighted by azimuthal density, to allow for uneven station distribution, and *SH* data were weighted to half of *P* data to allow for the greater amplitude of *S* waves. The widespread, routine use of this technique precludes the need for more detailed explanation (e.g. Molnar & Lyon-Caen 1989; Taymaz 1990).

Our estimated focal mechanism for the Minab earthquake is shown in Fig. 2, along with the seismograms used in the inversion and the associated synthetics for each station. The fault plane with strike 168° corresponds to the orientation of the right-lateral Minab–Zendan–Palami (MZP) fault zone; 160° (Regard *et al.* (2005); Fig. 1). However, from the InSAR data discussed below we find that the earthquake occurred on the orthogonal fault plane (strike 259°, dip 89°S and rake 5°). Our estimated centroid depth is 6 km. Based upon tests in which we hold one parameter at a value away from the best-fit, and re-invert the other parameters, we estimate the error in strike to be ±6°. Errors in the other quantities are asymmetric; dip lies in the range 79–89°, rake 0–12° and centroid depth 2–8 km. These are consistent with the typical errors found in other studies (e.g. Molnar & Lyon-Caen 1989).

We applied the same method to the two aftershocks of the Minab earthquake which had a sufficient signal-to-noise ratio to be analysed with this technique. These events were both predominantly strike-slip with nodal planes in approximately the same orientations as the main shock. Body waveform modelling solutions for these events are shown in Appendix A and their locations are discussed below.

3 CONSTANT SLIP INVERSION OF InSAR DATA

Radarsat-2 SAR interferograms spanning the time of the earthquake were produced by Samsonov & Czarnogorska (2013). In this section we invert the ground displacements in these interferograms for the source parameters of the Minab earthquake, for comparison with the seismological results described in Section 2 above. The descending and ascending track interferograms span 2012 November 1 to 2013 June 29, and 2012 November 6 to 2013 June 10, respectively. The

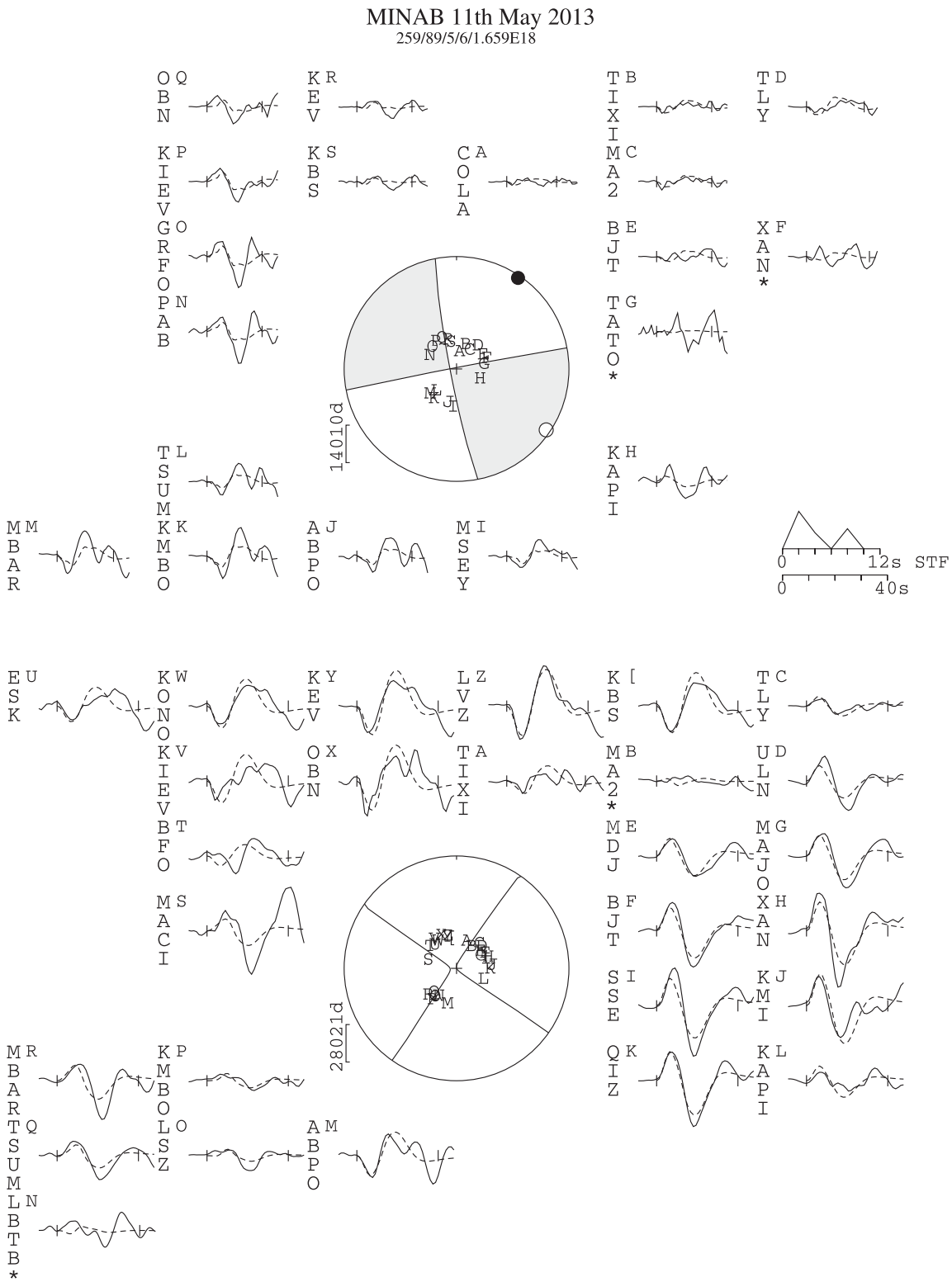

Figure 2. Lower hemisphere *P* (top) and *SH* (bottom) focal mechanisms from teleseismic body waves. Compressional quadrants are shaded for the *P* wave mechanism. Observed seismograms are shown by solid lines and the corresponding synthetics by dashed lines. *SH* waves are shown at half the magnification of *P* waves. Stations which were not included in the inversion, due to the low signal-to-noise ratio near nodal planes, are marked by an asterisk and the letter next to each seismogram is used to mark its projection onto the focal sphere. The parameters below the title are strike (°), dip (°), rake (°), depth (km) and seismic moment (Nm).

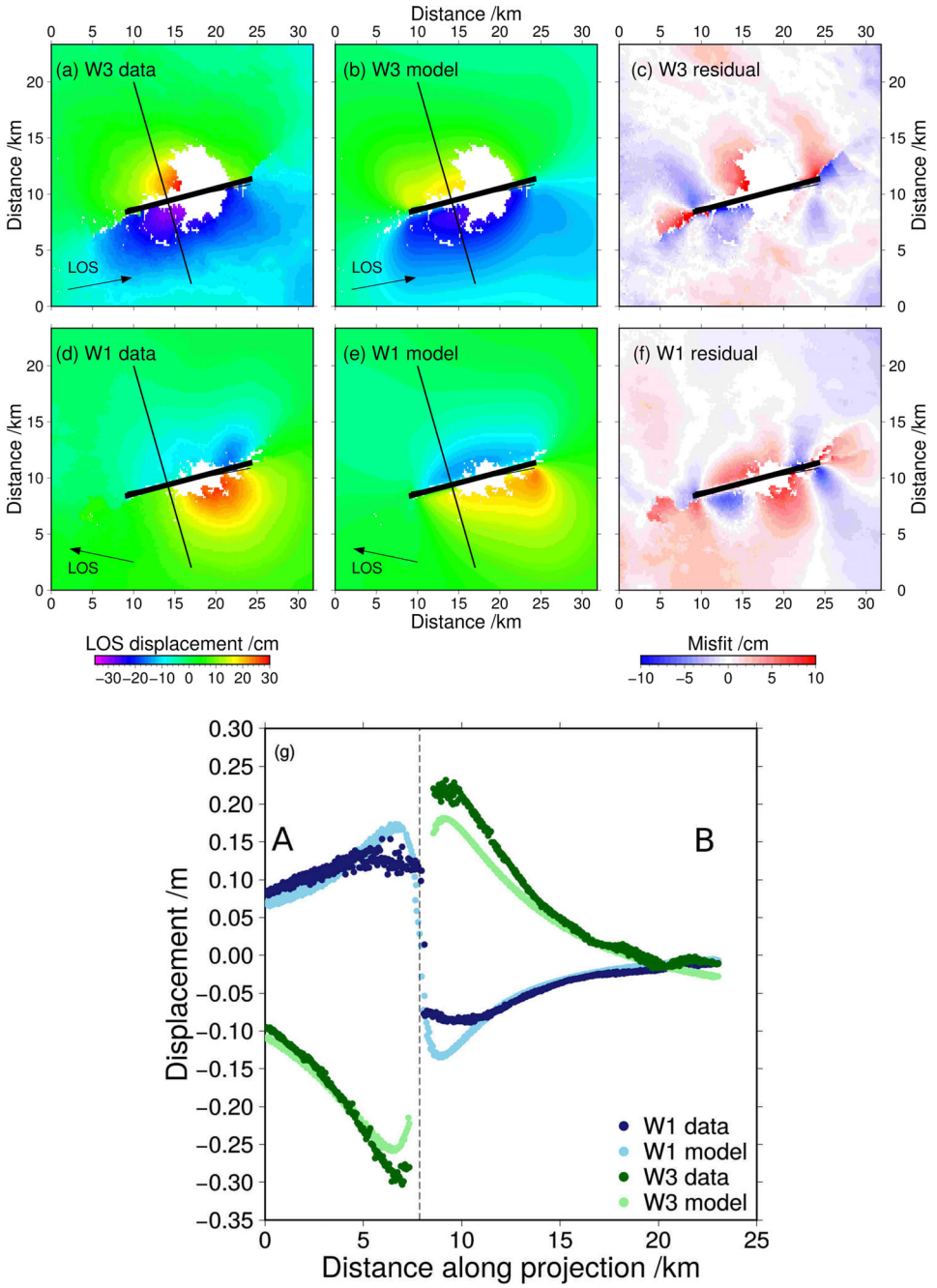

Figure 3. Results of the inversion of InSAR data for constant slip on a rectangular plane. (a) and (d) are the unwrapped ascending (top, W3) and descending (bottom, W1) SAR interferograms (Samsonov & Czarnogorska 2013), with the look direction of the satellite shown by the arrows labelled 'LOS'. Panels (b) and (e) show the best-fit model for each track, and (c) and (f) show the residual between the data and the model (calculated as the data minus the model). The thick black line in panels (a)–(f) is the surface projection of the fault plane. The thin, perpendicular line is the line of projection used in (g). (g) Ground displacements of data (dark colours) and models (light colours) S–N along the profile A–B shown in (a–f). The black, dashed line shows the intersection of the fault with the profile. The disparity between the models and the data near the fault is discussed in Section 3.

former includes 49 days of post-seismic data, the latter 30 days. The unwrapped interferograms are shown in Figs 3(a) and (d). The ∼E–W trending discontinuity in line-of-sight (LOS) displacements suggests rupture on an ∼E–W striking fault. The opposite senses of motion in the two interferograms (i.e. toward or away from the satellite) show that the measured ground motions are dominated by ∼E–W horizontal motions, which have opposite signs in ascending- and descending-track interferograms due to the different satellite look angles (marked on Fig. 3). We expect that the mainshock will dominate the ground motion signal as the largest reported aftershock, M_w 5.6, was nearly an order of magnitude smaller in seismic moment (see Appendix A). However, post-seismic slip may also contribute to the ground motions measured from InSAR, as discussed below.

The earthquake was modelled as a single plane with uniform slip, using the expressions of Okada (1985). We inverted for the depths of the top and bottom of the fault plane, strike, dip, rake, fault length, average slip and the geographical location of the fault. We

use an inversion routine based on a simulated annealing algorithm, in which the solution can move to higher misfits during the inversion, to avoid being trapped in local misfit minima. To increase the likelihood of finding the global minimum, we used the parameters derived from waveform modelling (Table 1) as a starting model, although the strike, dip and rake were allowed to take any values during the course of the inversion.

The results of the inversion are shown in Fig. 3. The inversion yields a fault plane with parameters given in Table 1. The motion is left-lateral strike-slip on an ENE–WSW striking plane, approximately orthogonal to the faults which have previously been mapped in this region (e.g. Peyret *et al.* 2009). The focal mechanism from this inversion is shown in Fig. 1(a) and is consistent both with our seismological solution and the focal mechanisms calculated by the CMT and NEIC. The source parameters are within error of those derived from teleseismic body waves, with the exception of the seismic moment, which is significantly larger from the slip inversion; 4.4×10^{18} N m (using a shear modulus of 28.3 GPa) as opposed to 1.7×10^{18} N m from seismology. This difference will be discussed in detail below. We find that the misfits between the model and the data are greatest near the fault. We suggest that this is due to the amount of slip in the earthquake decreasing towards the surface, a feature which cannot be captured in the constant-slip model used here. We return to this observation below, following inversions for the distribution of slip on the fault plane. The rms misfit between the model and the data for the constant slip inversion is 1.8 cm, similar to the amplitude of non-tectonic signals in areas of the interferogram away from the rupture (Fig. 3a).

4 DISTRIBUTED SLIP INVERSION OF InSAR DATA

We extend our analysis of the InSAR data set and invert for the distribution of slip on the fault geometry estimated in Section 3. We discretize the fault plane into 1.5 × 1.5 km cells. The SAR interferograms are then inverted for the slip on each patch using the simulated annealing method described by Ji *et al.* (2002). This method has been widely used for joint inversions of geodetic and seismological data (e.g. Konca *et al.* 2008, 2010) to obtain earthquake source models. Given the small size of the Minab earthquake, and the absence of a local seismic network, we did not attempt a joint inversion in this case as the teleseismic data would provide limited additional insight into the spatial distribution of fault slip. The velocity model used in this inversion (detailed in Table B1) is based on the structure obtained by Yamini-Fard *et al.* (2007) slightly north of our study area.

The trade-off between misfit and model roughness in inversion procedures is well-known (e.g. Jónsson & Zebker 2002). Following the approach of Freymueller *et al.* (1994) we select the solution in the apex of the curve relating misfit and model roughness, making the model as smooth as possible without significantly increasing the misfit. The dominant features of the resulting model do not vary within the section of the misfit curve corresponding to low misfit, physically plausible solutions (in which connected slip patches do not show large variations in slip magnitude or direction). The trade-off between misfit and smoothness is shown in Appendix B along with solutions that are rougher and smoother than the one presented here. In our preferred model, the rms misfit to the data is 1.7 cm.

We find a patch of slip extending from the surface to ∼10 km depth with an along-strike length of ∼20 km (Fig. 4a). The greatest slip is ∼1.85 m. The slip decreases towards the surface, as suggested by the near-fault misfits in our constant slip inversion (Section 3). The average slip from the constant slip inversion was 1.2 m, which agrees with the results of averaging over the slip patch in the distributed slip inversion. The seismic moment was allowed to vary in the inversion, with a starting value of 5×10^{18} N m, and converged on 4.5×10^{18} N m; similar to the constant slip inversion. The sense of motion of the patches is consistent with the nearly pure left-lateral slip found from body waveform modelling. The ∼20 km length of the fault plane is consistent with the ∼6 s length of the main part of the source-time function in our seismological inversions, if this represents the time to rupture the length of the fault at a velocity close to the *S* wave velocity (∼3.3 km s^{-1}).

5 FIELD OBSERVATIONS AND GEOMORPHOLOGY

Fig. 5 shows a satellite image of the fault that ruptured in the 2013 main shock. Ruptures were observed in the field between the two locations marked 'R'. The ruptures followed the obvious E–W trending valley, and were en-échelon right-stepping cracks, with a sense of motion consistent with left-lateral motion on the fault (Fig. 5). The surface displacements were on the order of centimetres. Such displacements are consistent with the decrease in slip towards the surface seen in the inversions of the InSAR data (Section 4). The magnitude of the surface slip was smaller than predicted from the geodetic results, which is a commonly observed feature thought to relate to the surface strain being distributed over a wide region of near-surface sediments, in addition to being focused as slip on a fault plane (e.g. Zinke *et al.* 2014). The fault is visible in the geomorphology (shown by white arrows in Fig. 5) and extends beyond the area where logistical constraints concentrated our field observations. The surface rupture locations, orientations and sense of slip are consistent with our estimated fault parameters based on our seismic and geodetic inversions.

The fault that ruptured in the 2013 event is characterized in the geomorphology by a linear valley that cuts across the strike of the geological units, and in places reverses the slopes of hillsides. Rivers draining from north to south across the area have sections which drain along the fault (blue lines on Fig. 5). These are not markers of the fault offset as they are larger than the offset of the geological contact between brown and green rocks marked on Fig. 5. The fault-parallel river courses are likely to be due to the fault rocks being more easily eroded than their surroundings, concentrating the drainage along the fault. These geomorphological characteristics allow other faults in the region to be identified. We focus on the region to the east of the MZP fault zone studied by Bayer *et al.* (2006), Peyret *et al.* (2009) and Masson *et al.* (2004), amongst others. A number of ∼E–W striking left-lateral strike-slip faults are visible in remote sensing data (marked as red lines on Figs 1b and 6). In common with the fault that ruptured in 2013, these faults are characterized by linear valleys, the reversal of hill slopes and the offset of geological units (examples of which are given in Appendix C). The tectonic significance of these faults is discussed below.

6 DISCUSSION

The 2013 Minab earthquake was almost entirely left-lateral strike-slip with strike 259°, dip 89° and rake 5°. The earthquake ruptured a patch ∼20 × 10 km^2 with slip decreasing towards the surface and maximum slip of ∼185 cm. The results from the seismic and geodetic inversions, and our field observations, are in agreement

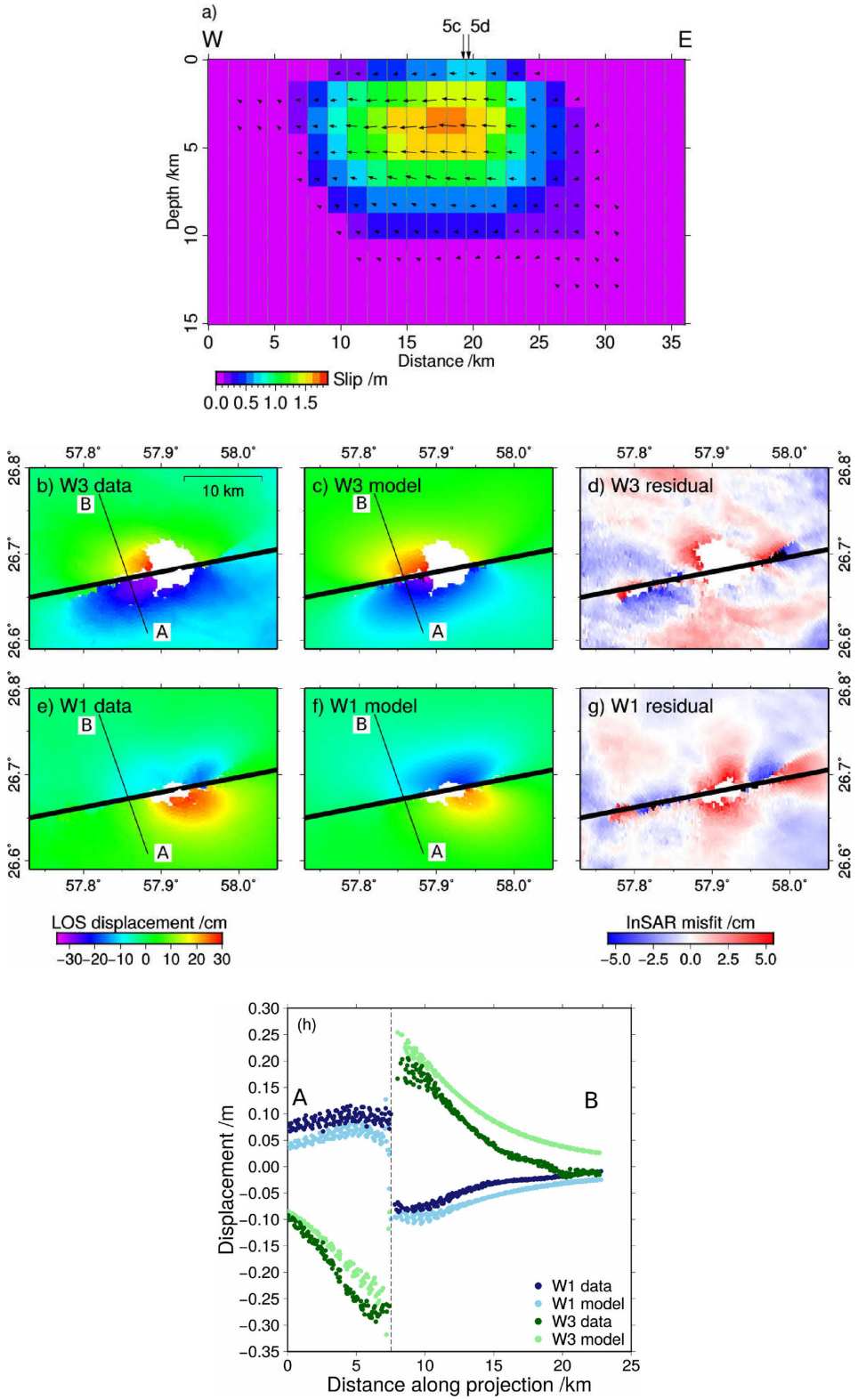

Figure 4. Results of distributed slip inversion for finite source. (a) shows slip distribution with depth in 1.5 × 1.5 km cells. The maximum slip is 1.9 m at ~4 km depth. The locations of Figs 5(c) and (d) are shown. (b)–(g) are as for Figs 3(a)–(f). (h) shows the displacements along the same profile as Fig. 3(g). The black, dashed line shows the intersection of the fault with the profile.

except in terms of the moment release. Our moment estimated from the body-wave inversions (1.7×10^{18} N m) is less than those from the geodetic inversions (4.4×10^{18} N m) and the gCMT solution (2.2×10^{18} N m), although it is similar to the NEIC value of 1.6×10^{18} N m. This may in part be due to the trade-off between source depth and moment. If the seismological centroid depth is forced to be 4 km (which lies within the error bounds on our solution), as implied by the geodetic results, then our estimated

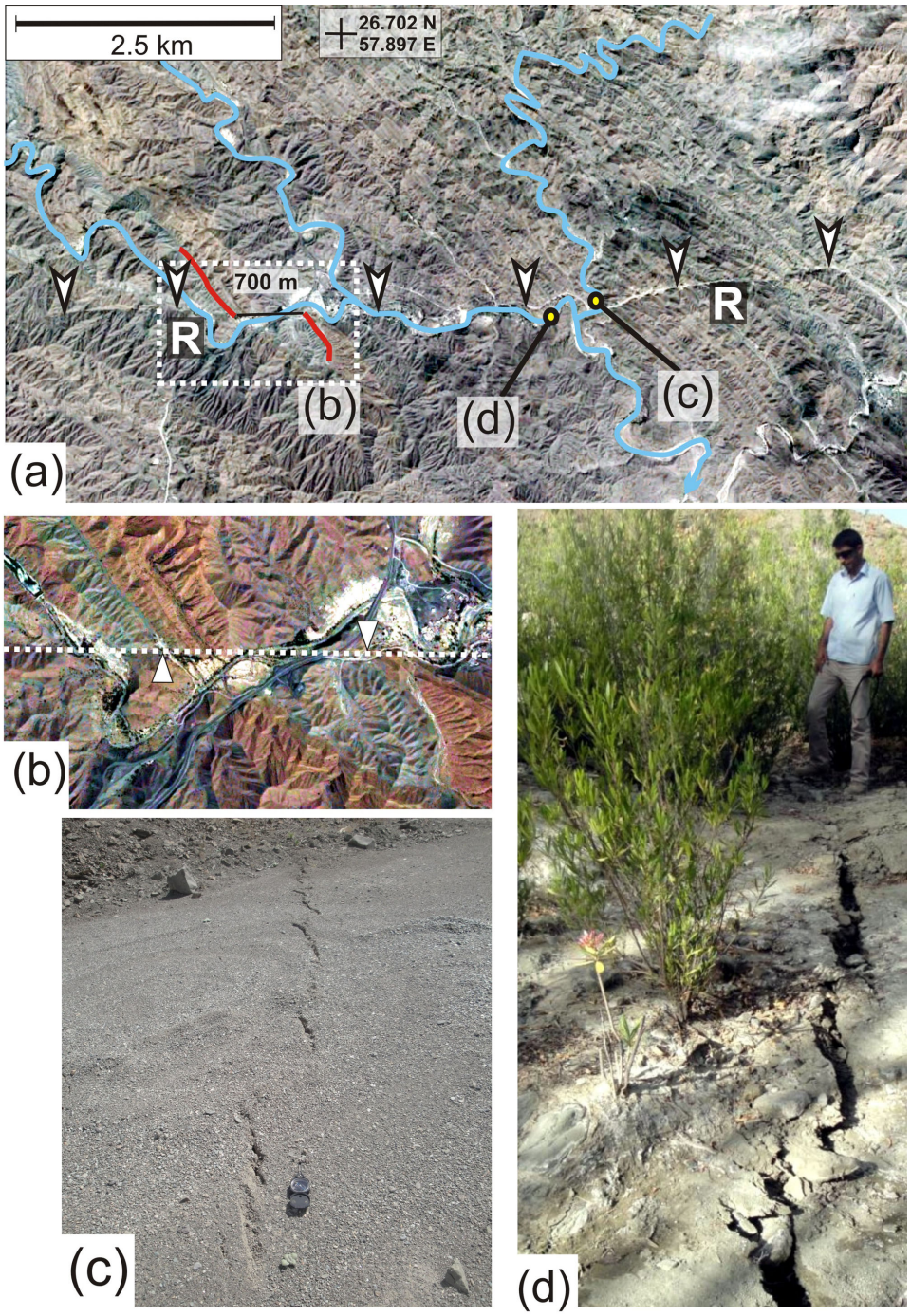

Figure 5. (a) Ikonos optical satellite image of the fault that ruptured in the 2013 mainshock. Image copyright Google Earth and DigitalGlobe. Surface ruptures were observed in the region between the two points marked 'R'. The white arrows show the location of the faulting visible in the geomorphology. The red line shows a contact between brown and green rocks that has been offset left-laterally by ~700 m. The rivers, shown in blue, do not reflect the geological offset (Section 5). White dashed box marks the area shown in (b). (b) Close up of offset geological contact with colours enhanced to highlight geological units (see also Appendix C). (c) and (d) show examples of the surface ruptures produced by the event from the points marked (c) and (d) in (a).

moment is 2.0×10^{18} N m, still significantly less than that from geodesy. It is likely that the inclusion of surface waveforms in the gCMT solution means that although that solution is less sensitive to the depth of the earthquake, and some components of the moment tensor (hence the benefits of our analysis above), the moment may be more accurate. However, there is relatively little difference between our seismological results and those of the CMT and NEIC.

The difference between seismological and geodetic estimates of earthquake magnitude is known from multiple other earthquakes in this region. For example, a series of thrust earthquakes on Qeshm Island in the Arabian Gulf had geodetic moments that were larger than those estimated using body waveform modelling by a factor of 1.5–5 (Nissen *et al.* 2010). A similar discrepancy of a factor of 2 was found for the 2006 Fin earthquake in the Iranian Zagros (Roustaei *et al.* 2010), and Lohman & Simons (2005) found

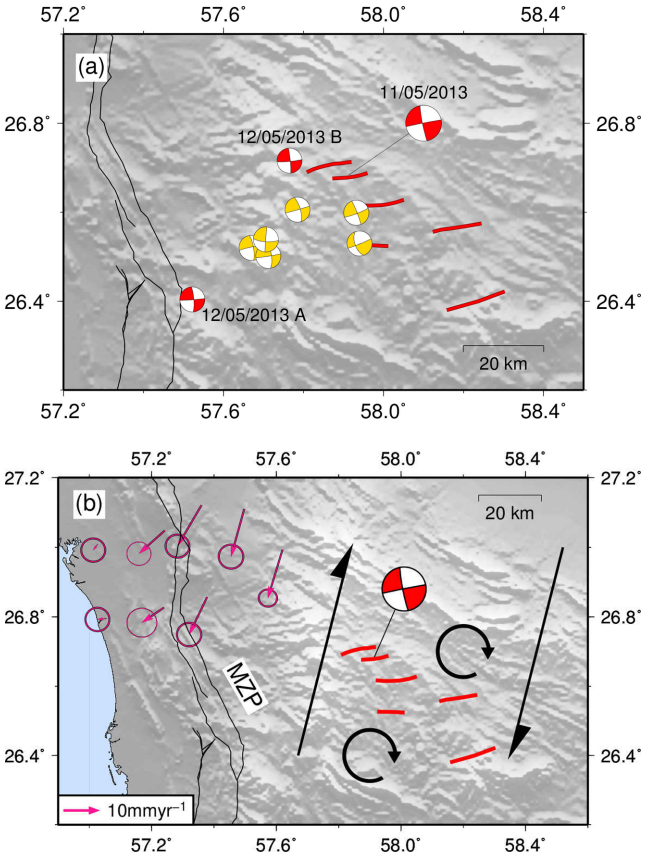

Figure 6. Seismicity and kinematics of source region. Lines in black (labelled MZP in (b)) are the Minab–Zendan–Palami fault zone from Regard *et al.* (2004). Lines in red are faults found in this study. (a) shows aftershock focal mechanisms at their NEIC epicentres. Compressional quadrants are shaded. The mechanism in red labelled 11/05/2013 is the body waveform modelling solution for the Minab mainshock from this study. Other red mechanisms are our body waveform modelling solutions for two aftershocks, as shown in Appendix A. Events in yellow are from the gCMT catalogue and have signal-to-noise ratios too low for body waveform modelling using the methods employed here. (b) shows an overview of the regional kinematics (discussed in Section 6.1). Vectors in pink are selected GPS relative to Arabia from Peyret *et al.* (2009) with ellipses showing 95 per cent confidence intervals. The GPS velocities show a W–E increase in southward velocity (see also Fig. 1b). Half arrows show schematically the overall shear across the region. Circular arrows show the sense of rotation (clockwise) of the left-lateral faults required to accommodate this shear.

systematically higher magnitude estimates from geodesy than seismology for a range of Zagros earthquakes. It therefore appears that the general pattern in the Zagros mountains of geodetically estimated moments being consistently larger than their seismic counterparts may extend eastwards into the Makran subduction zone. Following these previous authors we suggest that the discrepancy may relate to one of two effects: post-seismic slip or choice of velocity model. Post-seismic afterslip is sampled by InSAR observations, but not seismic waveforms, which could result in contrasting estimates of seismic moment. It is possible that the large thicknesses of sediment in the Zagros Mountains and Makran accretionary prism may lead to larger amounts of post-seismic slip compared to coseismic moment release than are commonly observed where faulting is contained within crystalline basement. If this slip occurred between 30 and 49 days after the earthquake, that is, in the interval between the acquisitions of the second images in the ascending and descending track interferograms, we would expect the slip models derived from both interferograms to overpredict the observed ground motion in the ascending track and underpredict the observed ground motion in the descending track. For the constant slip case, however, we find the opposite effect (Fig. 3g) with the model overpredicting slip for the descending track, which has more post-seismic data, and underpredicting slip for the ascending track, which has less post-seismic data. Post-seismic slip occurring between 30 and 49 days after the Minab earthquake is, therefore, not resolvable in this InSAR data. This does not preclude post-seismic slip in the period before the second set of SAR images were acquired. Alternatively, the difference in moment estimates between the seismic and geodetic models may result from systematic errors in the velocity model used, as suggested by Lohman & Simons (2005).

6.1 Regional tectonics

The fault that ruptured in the 2013 Minab earthquake and the other left-lateral strike-slip faults visible in the geomorphology (Fig. 6) are roughly perpendicular to the N160°E striking MZP fault zone. We also observe that the aftershocks of the Minab earthquake (shown in Fig. 6a) are all dominantly strike-slip, although the fault and auxiliary planes cannot be distinguished from seismology alone. The largest aftershock occurred near the mapped trace of the MZP so may have been right-lateral. However, several of the aftershocks have epicentres very close to the left-lateral faults expressed in the geomorphology, suggesting that these events are likely to have ruptured left-laterally. The tectonic significance of the fault which ruptured in the 2013 Minab event and the other E–W striking left-lateral strike-slip faults visible in the geology and geomorphology can be understood using the results of previous work on the active faulting and the GPS-derived velocity field of SE Iran. GPS results show that there is a velocity gradient equivalent to right-lateral shear on ∼N–S striking planes which extends from the Strait of Hormuz eastwards into the Makran (Fig. 1b; Peyret *et al.* 2009). This shear is partly accommodated by the faults of the MZP fault zone, which cumulatively slip at ∼4–8 mm yr^{-1} (Regard *et al.* 2005). However, this slip rate does not entirely account for the velocity differences of 23 and 19 mm yr^{-1} between the Strait of Hormuz and the GPS stations BAZM and CHAB respectively (labelled on Fig. 1b). We therefore suggest that the E–W striking left-lateral strike-slip faults we have studied accommodate at least part of the remainder of this motion by rotating clockwise about vertical axes (Fig. 6b). In order to achieve the overall rate of shear of 15–19 mm yr^{-1}, the faults would be required to slip at rates of ∼2.5–3.2 mm yr^{-1} (calculated using the expressions of Copley & Jackson (2006), and using block widths and lengths of 8 and 50 km, taken from Fig. 6). At such a rate, the geological offset of 700 m observed on the fault which ruptured in 2013 (Fig. 5) would require 0.2–0.3 Ma to accumulate and would allow the fault system as a whole to accommodate 4.2 km of N–S right-lateral shear. If the shear was evenly distributed east of the MZP fault zone, and the faults we have studied only accommodate the motion that occurs in the longitude range 57.6–58.4°, then the corresponding slip rates and ages would be 0.7 mm yr^{-1} and 1 Ma. Within the assumption of constant slip rates the 1.9 m of slip we observe in the 2013 Minab event would correspond to ∼3000 yr of slip accumulation. Clockwise rotations in the region east of the MZP fault zone are consistent with palaeomagnetic data (Aubourg *et al.* 2008).

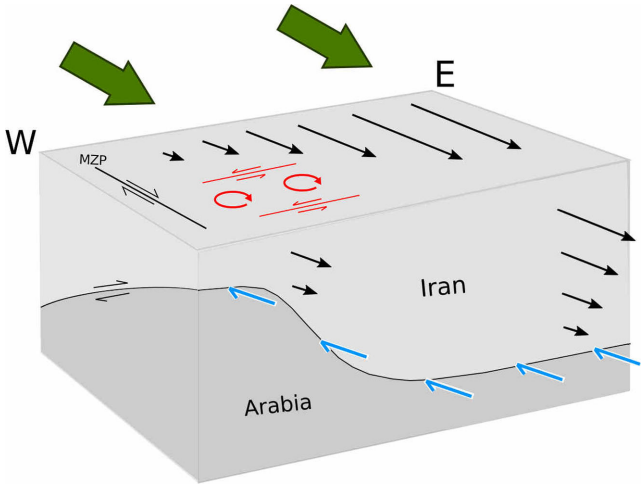

Figure 7. Schematic illustration of how the transition from continental to oceanic crust in the Arabian plate establishes a W–E velocity gradient at the surface. Green arrows show the overall compressive force across the region due to the convergence between Arabia and South Iran. Black arrows indicate velocities relative to Arabia with longer arrows corresponding to greater velocities. Blue half arrows indicate basal traction at the interface between Iran and Arabia. MZP is the Minab–Zendan–Palami fault zone and faults in red show the left-lateral faulting described in this study.

6.2 Relationship to Slab Geometry

Seismological studies (e.g. Kadinsky-Cade & Barazangi 1982; Yamini-Fard & Hatzfeld 2008) suggest that the Arabian plate is continuous across the Oman line, with no evidence for a slab tear. The transition from continental collision to subduction along the Arabian plate's northern boundary must, therefore, involve bending of the lithosphere towards the subduction zone along a W–E profile. The depth of the plate interface, combined with the traction transmitted across this interface, will exert a strong control on the surface motion. The traction across the plate interface sets the rate of shearing on horizontal planes within the upper plate. As the subduction interface deepens, the upper plate gets thicker so will be able to support a larger velocity difference between the underthrusting plate and the surface. The eastward deepening of the interface would, therefore, be expected to result in an eastward increase of convergence-parallel surface velocities relative to Arabia. When the slab flattens out (on a W–E cross section) then all points will have the same thickness of material over-riding the subduction interface, and the velocity at the surface would be expected to be constant along-strike. In this simple model, the right-lateral shear on N–S striking planes would be expected to extend eastwards from the Strait of Hormuz as far as the longitude at which the subducting plate achieves a constant depth along strike (see Fig. 7).

Yamini-Fard *et al.* (2007) conducted a survey of the seismicity and velocity structure in the region 56.5–58.5°E, 27–29.5°N. Between longitudes of 56.5° and 58° there is a W–E increase in seismic velocity across horizontal slices and a SW–NE deepening of seismicity. These results suggest that the subducting Arabian plate is progressively deepening eastward towards ∼58°E. Such deepening is consistent with the shear observed at the surface and the presence of the Minab earthquake fault and other E–W trending strike-slip faults over a region which approximately corresponds to this longitude range.

6.3 Strike-slip faulting in the accretionary wedge

The earthquake studied in this paper has some similarity to the 2013 M_w7.7 Balochistan earthquake (Avouac *et al.* 2014; Jolivet *et al.* 2014). Both events were strike-slip ruptures in the onshore part of the Makran accretionary prism. During the formation of the accretionary prism both of these regions would have been characterized by thrust faulting. However, both areas are now experiencing predominantly strike-slip faulting, and the Balochistan event is thought to have reactivated a dipping thrust fault in a strike-slip sense. A likely cause of the change in the style of faulting is the variation in gravitational potential energy which results from building topography (e.g. Dalmayrac & Molnar 1981; England & McKenzie 1982). The maximum elevation that a mountain range (or accretionary wedge) can reach depends on the forces acting to support the additional gravitational potential energy from thickening the crust (e.g. Molnar & Lyon-Caen 1988). These forces are related to the motion of the bounding plates, and in the case of the Makran accretionary wedge it is likely that maximum elevation of the wedge-top is limited by the stresses transmitted across the subduction zone megathrust. Once a wedge has reach its maximum elevation, thickening will migrate trenchward to the neighbouring lower parts of the wedge. The strike-slip earthquakes in Minab and Balochistan, the approximately flat top to the wedge in these regions and the active thrusting at lower elevations closer to the trench, suggest that the Makran wedge has reached the maximum elevation that can be supported by the stresses transmitted across the subduction megathrust.

7 CONCLUSIONS

We have studied the May 2013 M_w 6.1 Minab earthquake. Left-lateral strike-slip motion on a plane oriented ∼E–W broke one of a series of left-lateral strike-slip faults within the Makran accretionary prism. These faults accommodate an overall velocity field equivalent to right-lateral shear on ∼N–S striking planes. The cause of this shear, which extends ∼200 km east of the Strait of Hormuz, is likely to be the tractions relating to the underthrusting Arabian lithosphere, which deepens over this longitude range.

ACKNOWLEDGEMENTS

We thank the editor and two anonymous reviewers for comments on the manuscript, and Jean-Philippe Avouac and James Jackson for useful discussions. This work forms part of the NERC and ESRC funded project 'Earthquakes Without Frontiers'. CP is funded by an NERC PhD studentship.

REFERENCES

Aubourg, C., Smith, B., Bakhtari, H.R., Guya, N. & Eshraghi, A., 2008. Tertiary block rotations in the Fars Arc (Zagros, Iran), *Geophys. J. Int.,* **173**(2), 659–673.

Avouac, J.-P. *et al.*, 2014. The 2013, Mw 7.7 Balochistan earthquake, energetic strike-slip reactivation of a thrust fault, *Earth planet. Sci. Lett.,* **391,** 128–134.

Bayer, R. *et al.*, 2006. Active deformation in Zagros-Makran transition zone inferred from GPS measurements, *Geophys. J. Int.,* **165**(1), 373–381.

Copley, A. & Jackson, J., 2006. Active tectonics of the Turkish-Iranian Plateau, *Tectonics,* **25**(6), doi:10.1029/2005TC001906.

Dalmayrac, B. & Molnar, P., 1981. Parallel thrust and normal faulting in Peru and constraints on the state of stress.*Earth planet. Sci. Lett.,* **55**(3), 473–481.

Dziewonski, A.M., Chou, T.-A. & Woodhouse, J.H., 1981. Determination of earthquake source parameters from waveform data for studies of global and regional seismicity, *J. geophys. Res.,* **86**(B4), 2825–2852.

Ekström, G., Nettles, M. & Dziewonski, A.M., 2012. The global CMT project 2004 2010: Centroid-moment tensors for 13,017 earthquakes, *Phys. Earth planet. Inter.,* **200–201,** 1–9.

England, P. & McKenzie, D., 1982. A thin viscous sheet model for continental deformation, *Geophys. J. Int.,* **70**(2), 295–321.

Freymueller, J., King, N. & Segall, P., 1994. The co-seismic slip distribution of the Landers earthquake, *Bull. seism. Soc. Am.,* **84**(3), 646–659.

Ji, C., Wald, D. & Helmberger, D., 2002. Source description of the 1999 Hector Mine, California, earthquake, part I: Wavelet domain inversion theory and resolution analysis, *Bull. seism. Soc. Am.,* **92**(4), 1192–1207.

Jolivet, R. *et al.*, 2014. The 2013 Mw 7.7 Balochistan Earthquake: Seismic Potential of an Accretionary Wedge, *Bull. seism. Soc. Am.,* **104**(2), 1020–1030.

Jónsson, S. & Zebker, H., 2002. Fault slip distribution of the 1999 Mw 7.1 Hector Mine, California, earthquake, estimated from satellite radar and GPS measurements, *Bull. seism. Soc. Am.,* **92**(4), 1377–1389.

Kadinsky-Cade, K. & Barazangi, M., 1982. Seismotectonics of southern Iran: the Oman line, *Tectonics,* **1**(5), 389–412.

Konca, O. *et al.*, 2008. Partial rupture of a locked patch of the Sumatra megathrust during the 2007 earthquake sequence, *Nature,* **456**(7222), 631–635.

Konca, O., Leprince, S., Avouac, J.-P. & Helmberger, D.V., 2010. Rupture process of the 1999 Mw 7.1 Duzce earthquake from joint analysis of SPOT, GPS, InSAR, strong-motion, and teleseismic data: a supershear rupture with variable rupture velocity, *Bull. seism. Soc. Am.,* **100**(1), 267–288.

Lohman, R.B. & Simons, M., 2005. Locations of selected small earthquakes in the Zagros mountains, *Geochem. Geophys. Geosyst.,* **6,** doi:10.1029/2004GC000849.

Masson, F., Chéry, J., Hatzfeld, D., Martinod, J., Vernant, P., Tavakoli, F. & Ghafory-Ashtiani, M., 2004. Seismic versus aseismic deformation in Iran inferred from earthquakes and geodetic data, *Geophys. J. Int.,* **160**(1), 217–226.

McCaffrey, R. & Abers, G., 1988. SYN3: a program for inversion of teleseismic body waveforms on microcomputers, Tech. rep., Air Force Geophysics Laboratory Technical Report.

McCaffrey, R., Abers, G. & Zwick, P., 1991. Inversion of teleseismic body waves, in *Digital Seismogram Analysis and Waveform Inversion,* pp. 81–166, ed. Lee, W., Int. Assoc. Seismol. Phys. Earth Inter. Software Library.

Molnar, P. & Lyon-Caen, H., 1988. Some simple physical aspects of the support, structure, and evolution of mountain belts. *GSA Spec. Pap.,* **218,** 179–208.

Molnar, P. & Lyon-Caen, H., 1989. Fault plane solutions of earthquakes and active tectonics of the Tibetan Plateau and its margins, *Geophys. J. Int.,* **99**(1), 123–154.

Nissen, E., Yamini-Fard, F., Tatar, M., Gholamzadeh, A., Bergman, E., Elliott, J., Jackson, J. & Parsons, B., 2010. The vertical separation of mainshock rupture and microseismicity at Qeshm island in the Zagros fold-and-thrust belt, Iran, *Earth planet. Sci. Lett.,* **296**(3–4), 181–194.

Nissen, E., Tatar, M., Jackson, J. & Allen, M., 2011. New views on earthquake faulting in the Zagros fold-and-thrust belt of Iran, *Geophys. J. Int.,* **186**(3), 928–944.

Okada, Y., 1985. Surface deformation due to shear and tensile faults in a half-space, *Bull. seism. Soc. Am.,* **75**(4), 1135–1154.

Peyret, M. *et al.*, 2009. Present-day strain distribution across the Minab-Zendan-Palami fault system from dense GPS transects, *Geophys. J. Int.,* **179**(2), 751–762.

Regard, V., Bellier, O., Thomas, J.-C., Abbassi, M.R., Mercier, J., Shabanian, E., Feghhi, K. & Soleymani, S., 2004. Accommodation of Arabia-Eurasia convergence in the Zagros-Makran transfer zone, SE Iran: a transition between collision and subduction through a young deforming system, *Tectonics,* **23**(4), doi:10.1029/2003TC001599.

Regard, V. *et al.*, 2005. Cumulative right-lateral fault slip rate across the Zagros-Makran transfer zone: role of the Minab-Zendan fault system in accommodating Arabia-Eurasia convergence in southeast Iran, *Geophys. J. Int.,* **162**(1), 177–203.

Roustaei, M. *et al.*, 2010. The 2006 March 25 Fin earthquakes (Iran)-insights into the vertical extents of faulting in the Zagros Simply Folded Belt, *Geophys. J. Int.,* **181**(3), 1275–1291.

Samsonov, S.V. & Czarnogorska, M., 2013. Ground deformation produced by 2013 M6.1 Minab earthquake in Iran mapped with RADARSAT-2 InSAR, Geological Survey of Canada Open File 7528, 7p.

Taymaz, T., 1990. Earthquake mechanisms in the Hellenic Trench near Crete, *Geophys. J. Int.,* **102**(3), 695–731.

Vernant, P. *et al.*, 2004. Present-day crustal deformation and plate kinematics in the Middle East constrained by GPS measurements in Iran and northern Oman, *Geophys. J. Int.,* **157**(1), 381–398.

Yamini-Fard, F. & Hatzfeld, D., 2008. Seismic structure beneath Zagros-Makran transition zone (Iran) from teleseismic study: seismological evidence for underthrusting and buckling of the Arabian plate beneath central Iran, *JSEE,* **10**(1), 11–24.

Yamini-Fard, F., Hatzfeld, D., Farahbod, A.M., Paul, A. & Mokhtari, M., 2007. The diffuse transition between the Zagros continental collision and the Makran oceanic subduction (Iran): microearthquake seismicity and crustal structure, *Geophys. J. Int.,* **170**(1), 182–194.

Zinke, R., Hollingsworth, J. & Dolan, J., 2014. Slip and off fault deformation patterns in the 2013 MW 7.7 Balochistan, Pakistan earthquake: implications for controls on the distribution of near surface coseismic slip, *Geochem. Geophys. Geosyst.,* **15**(12), 5034–5050.

Zwick, P., McCaffrey, R. & Abers, G., 1994. MT5 program, in *IASPEI Software Library, number 4, IASPEI*.

APPENDIX A: BODY WAVEFORM MODELLING OF AFTERSHOCKS

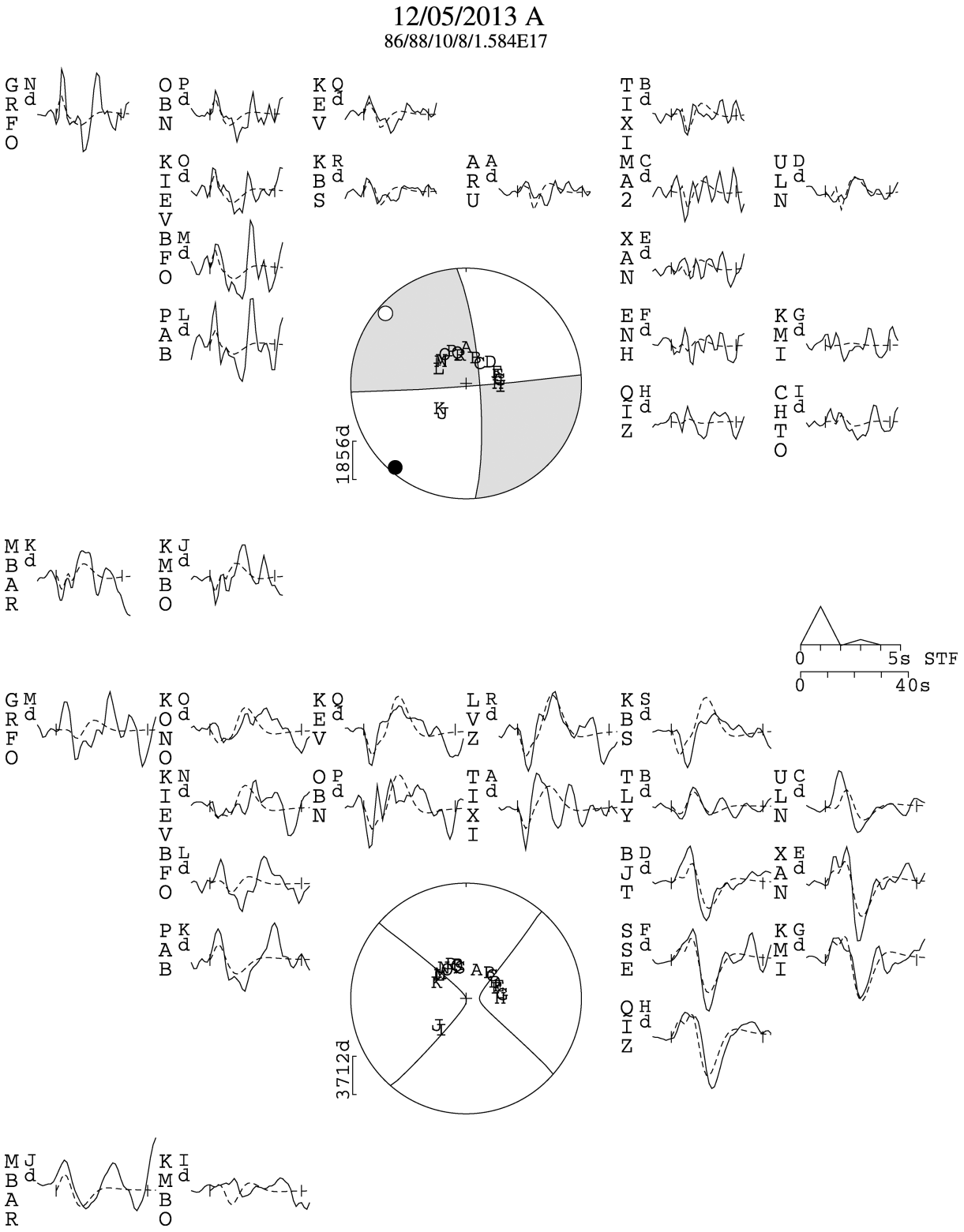

Figure A1. *P* (top) and *S* (bottom) lower hemisphere focal mechanisms from body waveform modelling for the largest aftershock of the Minab earthquake. The two nodal planes have strike 86°, dip 88° and rake 10°, and strike 356°, dip 80° and rake 178°, respectively.

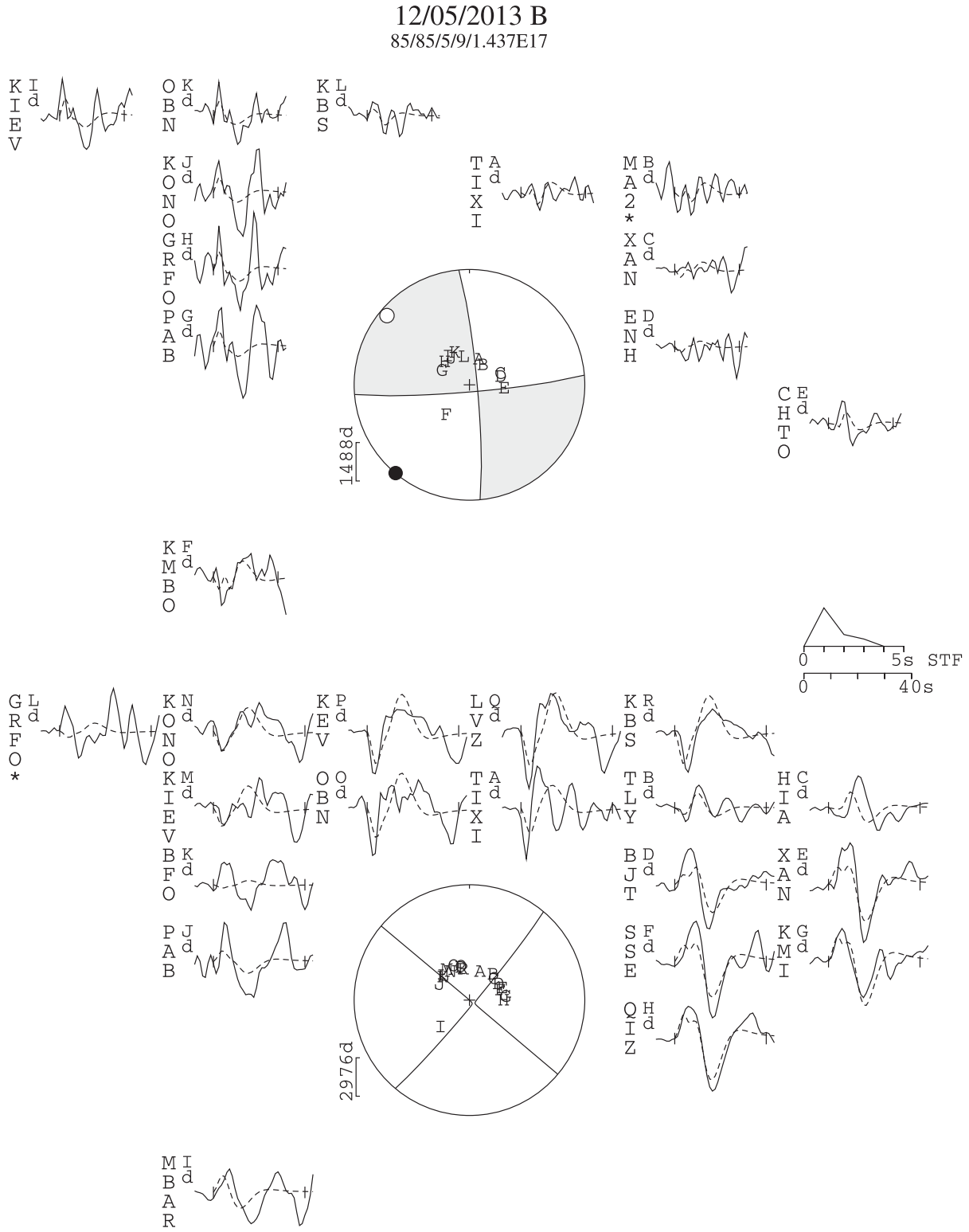

Figure A2. *P* (top) and *S* (bottom) lower hemisphere focal mechanisms from body waveform modelling for an aftershock of the Minab earthquake. The two nodal planes have strike 85°, dip 85° and rake 5°, and strike 355°, dip 85° and rake 175°, respectively.

APPENDIX B: DISTRIBUTED SLIP INVERSION: VELOCITY MODEL AND MISFIT-ROUGHNESS TRADE-OFF

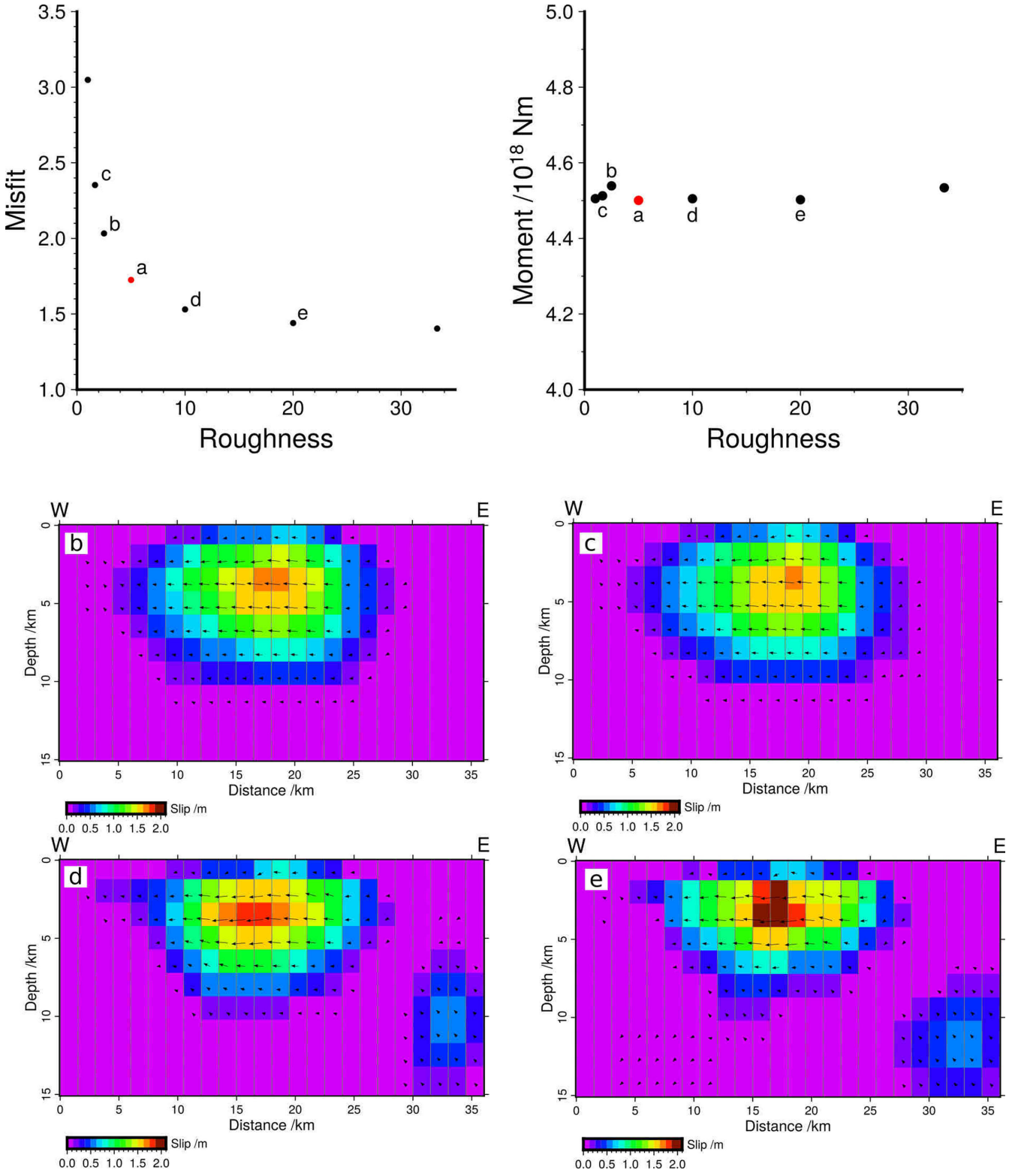

Figure B1. The top left panel shows the relationship between misfit and model roughness in our inversion of InSAR data for the distribution of slip on the fault plane. Our preferred model, shown in Fig. 4(a), is marked in red and labelled a. The corresponding slip distributions for the points labelled b–e are shown in the lower panels; b and c represent smoother solutions than our chosen one and d and e represent rougher solutions. The moment from the different inversions is shown in the top right panel. Within the apex of the Misfit–Roughness curve there is good agreement with a moment of 4.5×10^{18} N m.

Table B1. Velocity model used for distributed slip inversion.

Depth to base (km)	V_p (km s^{-1})	V_s (km s^{-1})	μ (GPa)
11	5.6	3.3	28.3
21	6.6	3.8	39.0
30	6.9	4.0	44.8
–	8.1	4.5	66.8

APPENDIX C: GEOLOGICAL AND GEOMORPHOLOGICAL INDICATORS OF ACTIVE FAULTING

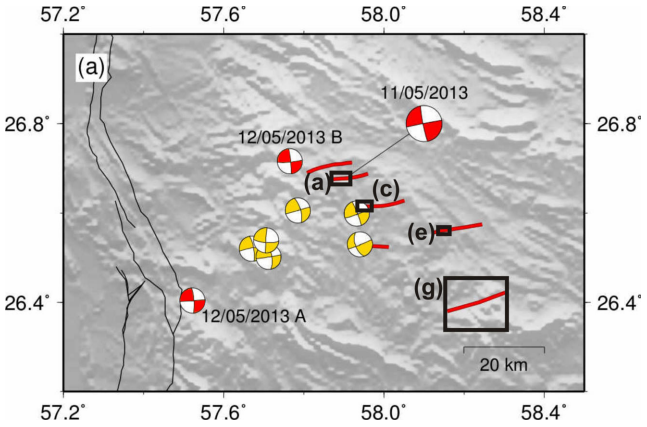

Figure C1. As for Fig. 6(a) from the main paper, with the addition of boxes showing the areas of coverage of the satellite images in Fig. C2.

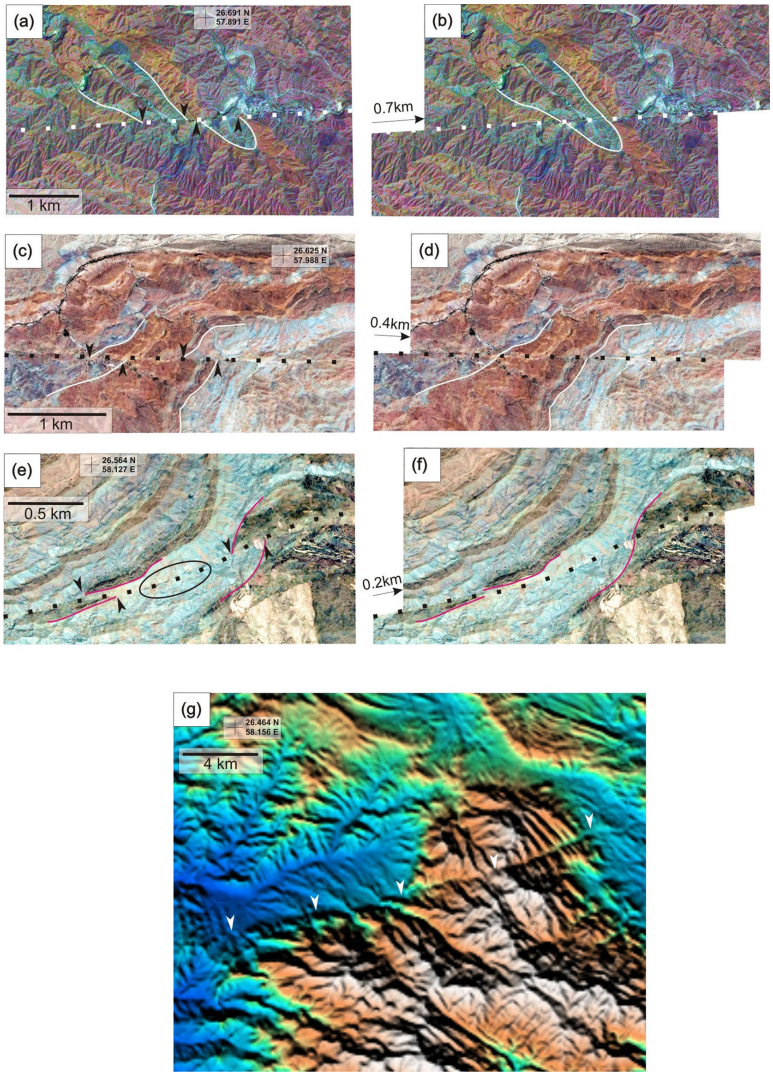

Figure C2. Panels (a), (c) and (e) show satellite images of fault offsets in the locations indicated in Fig. C1. Panel (a) corresponds to the western part of Fig. 5(a) in the main paper. Offset geological units are marked by black arrows and white or pink lines. Panels (b), (d) and (f) show the same locations with the left-lateral offsets reconstructed by reversing the fault motion by the amount indicated on the figure. Panel (g) shows an example of the geomorphology in the region indicated on Fig. C1. The location of the fault is shown by white arrows, and cuts across the strike of the geological units. The western part of the fault forms a sharp range-front, and the eastern part results in linear valleys which cut across the geological structures and other drainage (e.g. in the region of anticlines in the east of the image).